Mechanistic insights into red mud, blast furnace slag, or metakaolin-assisted stabilization/solidification of arsenic-contaminated sediment

Lei Wang[a,b], Liang Chen[a], Daniel C.W. Tsang[a,*], Yaoyu Zhou[a,c], Jörg Rinklebe[d,e], Hocheol Song[e], Eilhann E. Kwon[e], Kitae Baek[f], Yong Sik Ok[g,*]

[a] Department of Civil and Environmental Engineering, The Hong Kong Polytechnic University, Hung Hom, Kowloon, Hong Kong, China
[b] Department of Materials Science and Engineering, The University of Sheffield, Sir Robert Hadfield Building, Mappin St, Sheffield S1 3JD, United Kingdom
[c] College of Resources and Environment, Hunan Agricultural University, Changsha 410128, China
[d] University of Wuppertal, School of Architecture and Civil Engineering, Soil- and Groundwater-Management, Pauluskirchstraße 7, D-42285 Wuppertal, Germany
[e] Sejong University, Department of Environment, Energy and Geoinformatics, 98 Gunja-Dong, Guangjin-Gu, Seoul, South Korea
[f] Department of Environmental Engineering and Soil Environment Research Center, Chonbuk National University, 567 Baekje-daero, Deokjin, Jeonju, Jeollabukdo 561-756, South Korea
[g] Korea Biochar Research Center, Division of Environmental Science and Ecological Engineering, Korea University, Seoul 02841, South Korea

ARTICLE INFO

ABSTRACT

Elevated level of arsenic (As) in marine sediment via deposition and accumulation presents long-term ecological risks. This study proposed a sustainable stabilization/solidification (S/S) of As-contaminated sediment via novel valorization of red mud waste, blast furnace slag and calcined clay mineral, which were selected to mitigate the increased leaching of As under alkaline environment of S/S treatment. Quantitative X-ray diffraction and thermogravimetric analyses illustrated that stable Ca-As complexes (e.g., $Ca_5(AsO_4)_3OH$) could be formed at the expense of $Ca(OH)_2$ consumption, which inevitably hindered the hydration process and S/S efficiency. The ^{29}Si nuclear magnetic resonance analysis revealed that incorporation of metakaolin for As immobilization resulted in a low degree of hydration and polymerization, whereas addition of red mud promoted Fe-As complexation and demonstrated excellent compatibility with As. Transmission electron microscopy and elemental mapping further confirmed the precipitation of crystalline Ca-As and amorphous Fe-As compounds. Therefore, red mud-incorporated S/S binder achieved the highest efficiency of As immobilization (99.9%), which proved to be applicable for both *in-situ* and *ex-situ* S/S of As-contaminated sediment. These results advance our mechanistic understanding for the design of green and sustainable remediation approach for effective As immobilization.

1. Introduction

Arsenic (As) is a toxic and carcinogenic oxyanionic element that is ubiquitous in the natural environment. Anthropogenic activities (including mineral exploitation, chemical manufacture, coal combustion, and sewage irrigation) aggravate the As pollution in ecosystems (Hammond et al., 2018). The presence of As even at a very low level would pose severe human health effects, such as skin, lungs, kidney and liver cancers (Smith et al., 2018). Contaminants from surface runoff, atmospheric deposition, as well as industrial/municipal sewage discharge often deposit and accumulate in the sediment of the receiving water bodies, as illustrated by the detection of elevated level of As in offshore marine sediment (Aghadadashi et al., 2019; Liu et al., 2019; Sun et al., 2019a, 2019b). Recent studies illustrated the risk of As release from contaminated sediment back into water column upon the change of physicochemical conditions of the sediment-water system (Le Monte et al., 2017; Ding et al., 2018; Bettosch et al., 2018). To reduce the As concentration and mobility, *in-situ* or *ex-situ* remediation of contaminated sediment is required (Garcia-Ordiales et al., 2018; Cui and Jing, 2019). Various sediment remediation technologies have been

explored, such as iron/manganese adsorption and chemical-enhanced extraction (Liu et al., 2018; Yoo et al., 2018; Cai et al., 2019). However, the addition of iron/manganese may cause secondary pollution, whereas technical and financial constraints limit the full-scale application of chemical-enhanced extraction (Beiyuan et al., 2017a; Chen et al., 2019a, 2019b; Maletić et al., 2019). Therefore, the development of time-saving, cost-effective, and sustainable approach to remediate As-contaminated sediments is a research priority.

Stabilization/solidification (S/S) is a mature and widely accepted technology for the treatment of hazardous materials for its high efficiency and easy implementation (Shen et al., 2018; Wang et al., 2018a; Zhang et al., 2018a, 2018b). Toxic elements can be physically encapsulated and/or chemically fixed in the solidified matrixes via cement hydration or alkaline activation (Reddy et al., 2019; Wang et al., 2019a). Although ordinary Portland cement (PC) has an outstanding immobilization ability for cationic metals (e.g., Cu, Zn, Cd, and Pb) (Kim and Lee, 2017; Wang et al., 2018a; Chen et al., 2019a, 2019b), the immobilization efficiency for metalloids (e.g., As) should be further validated and new binder materials and designs should be investigated because the highly alkaline and high-salinity environment of cementitious matrixes would induce higher As leaching after the S/S process (Li et al., 2018; Wang et al., 2019b).

The encapsulation and precipitation efficiency can be enhanced by (i) the generation of additional cement hydrates or (ii) the incorporation of As stabilizers. In particular, blast furnace slag (BS, a by-product from iron and steel-making industry) is a supplementary cementitious material (SCM) that can react with excessive hydrated calcium hydroxide (CH) to generate secondary hydrates via pozzolanic reaction (Myers et al., 2017; Ruan and Unluer, 2017; Prentice et al., 2019; Xie et a., 2019). Metakaolin (MK, produced from calcination of kaolinite) is regarded as a low-cost and low-carbon SCM for it releases less CO_2 during manufacture (0.18 tonne CO_2 per tonne MK) compared to PC production (0.82 tonne CO_2 per tonne PC) (Kavitha et al., 2016; Provis, 2018; He et al., 2019). Similarly, MK could be activated by CH to generate additional hydrates such as calcium silicate hydrate (CSH) and calcium aluminium hydrate (CAH) (Avet et al., 2018; Gbozee et al., 2018; Wang et al., 2018b). These additional hydrates may be favourable for the encapsulation of As and densification of the structure of S/S products. In addition, As(III) and As(V) are known to strongly bind with iron oxides/hydroxides by inner-sphere complexation for their effective removal (Tian et al., 2016; Sun et al., 2018; Sun et al., 2019a, 2019b). Therefore, Fe-rich red mud (RM, an alumina refinery residue) has a potential to enhance the efficiency of As immobilization as a stabilizer against alkalinity-induced leaching. However, it remains uncertain if the two approaches (i.e., supplementary hydration or As stabilization) are equally effective or else. Our mechanistic understanding of the relative significance is still in lack so far.

In order to provide mechanistic insights for developing a green and sustainable S/S technology for As-contaminated sediment, this study aims to: (i) elucidate the chemical interactions between hydrates and As; (ii) assess the mechanistic roles of green materials (BS, MK, and RM) for enhancing hydrate formation and/or As precipitation; and (iii) investigate the environmental feasibility of waste-incorporated binders for *in-situ* and *ex-situ* S/S of As-contaminated sediment.

2. Materials and methods

2.1. Materials

The marine sediment was dredged from the surface (top 0.5 m) of the Kai Tak Approach (10 m of water depth) in Victoria Harbour in Hong Kong. The sediment samples had a moisture content of 59.8%, pH value of 7.2, salinity of 35.9 g kg^{-1}, organic matter of 6.9% (combustion at 550 °C). The sediment was composted of 27% gravel, 58% sand, and 15% silt and clay as determined by wet sieving and hydrometer tests (Wang et al., 2015). Due to historical pollution from the former

Table 1
Chemical compositions of cementitious materials (wt%).

	Na$_2$O	MgO	Al$_2$O$_3$	SiO$_2$	P$_2$O$_5$	SO$_3$	K$_2$O	CaO	Fe$_2$O$_3$
PC	0.17	1.38	4.79	18.99	0.08	4.52	0.79	65.72	3.10
BS	0.00	6.19	15.35	35.34	0.04	2.37	0.85	38.33	0.31
MK	0.00	0.00	47.00	50.30	0.28	0.05	0.28	0.18	0.52
RM	2.78	0.11	16.16	9.11	0.37	0.56	1.56	2.17	59.37

PC: ordinary Portland cement; BS: blast furnace slag; MK: metakaolin; RM: red mud.

Kai Tak Airport and nearby industrial zone, the sediment was highly contaminated by potentially toxic elements, such as Cu (1600 mg kg^{-1}), Zn (410 mg kg^{-1}), Cr (230 mg kg^{-1}), As (201 mg kg^{-1}), Pb (130 mg kg^{-1}), Ni (65 mg kg^{-1}), and Cd (2.4 mg kg^{-1}) (HK EPD, 2018). Among them, As was regarded as one of the most unextractable elements by conventional treatments (Wang et al., 2019b). The sediment was classified as highly contaminated sediment (Category H) according to the sediment management guideline in Hong Kong.

The primary cementitious material was ordinary Portland cement (ASTM Type I) purchased from Green Island Cement Company in Hong Kong. Besides, BS from Shengheng Mineral Company in China, MK from Super Cnpowder Technology Company in China, and RM as a waste from Weiqiao Aluminium Industry were employed as SCMs. The chemical compositions of cementitious materials determined by X-ray fluorescence (XRF) are shown in Table 1, and these materials have a comparable particle size (< 0.125 mm). Reagent grade NaAsO$_2$ was purchased from Sigma-Aldrich, Hong Kong. It should be noted that to simulate field-relevant engineering applications, seawater instead of tap water was added for the S/S treatment in this study.

2.2. Sample preparation

Binder with 100% PC was marked as PC group (control), and different green alternatives (BS, MK, and RM) were used to partially replace PC by 20 wt% in other three groups. To investigate the S/S mechanisms of different binders, reagent grade NaAsO$_2$ (20 wt% of binder) was added into mixtures, because As(III) is more toxic and more difficult to be immobilized compared to As(V) (Table 2). For As-incorporated pastes production, NaAsO$_2$ was dissolved in seawater to form a homogeneous solution and subsequently poured into pre-mixed binders (PC, BS, MK or RM) for 2 min fast mixing. The fresh mixtures were then poured into 15 mL centrifuge tubes and vibrated for 1 min to release air bubbles. The sealed tubes were stored in an incubator at 23 ± 1 °C for 28-d curing before analyses. The sediment-to-binder mass ratios at 7:3 and 9:1 were selected for *in-situ* and *ex-situ* sediment S/S, respectively. The waste-incorporated binders were made with the same procedure as described above. Pre-mixed binders were poured into the sediment and stirred for another 2 min to form homogenous matrixes. The fresh matrixes were filled into steel moulds (5 × 5 × 5 cm^3) and vibrated in a vibration table for 1 min to release air bubbles. After 1-d curing, the hardened sediment blocks were demoulded and then were wrapped with a plastic membrane. Afterwards, samples were stored in an incubator at 23 ± 1 °C for 7-d and 28-d air curing. All the experiments on As-pastes and sediment S/S blocks were triplicated for quality assurance.

2.3. Analytical methods

The compositions of powdered samples were analysed by thermogravimetric analysis (TGA, Rigaku Thermo Plus) with an elevated temperature from 100 to 1000 °C at a heating rate of 10 °C min^{-1} with Ar carrier gas. Mineralogy of the powdered S/S samples was measured by quantitative X-ray diffraction (QXRD) using an X-ray diffractometer (Rigaku SmartLab) with a scan range from 15° to 50° 2θ at 2.5° min^{-1}.

Table 2
Mixture formulations of different As and sediment blocks (by weight).

	Binder formations					S/S of As	In-situ S/S	Ex-situ S/S
	PC	BS	MK	RM	Sea water	NaAsO$_2$[a]	Wet sediment[b]	Semi-wet sediment[c]
PC groups	100	0	0	0	30	20	900	233
BS groups	80	20	0	0	30	20	900	233
MK groups	80	0	20	0	30	20	900	233
RM groups	80	0	0	20	30	20	900	233

[a] Moisturizing with additional sea water (30 wt% of NaAsO$_2$).
[b] Sediment with 60 wt% of water content.
[c] Sediment with 30 wt% of water content.
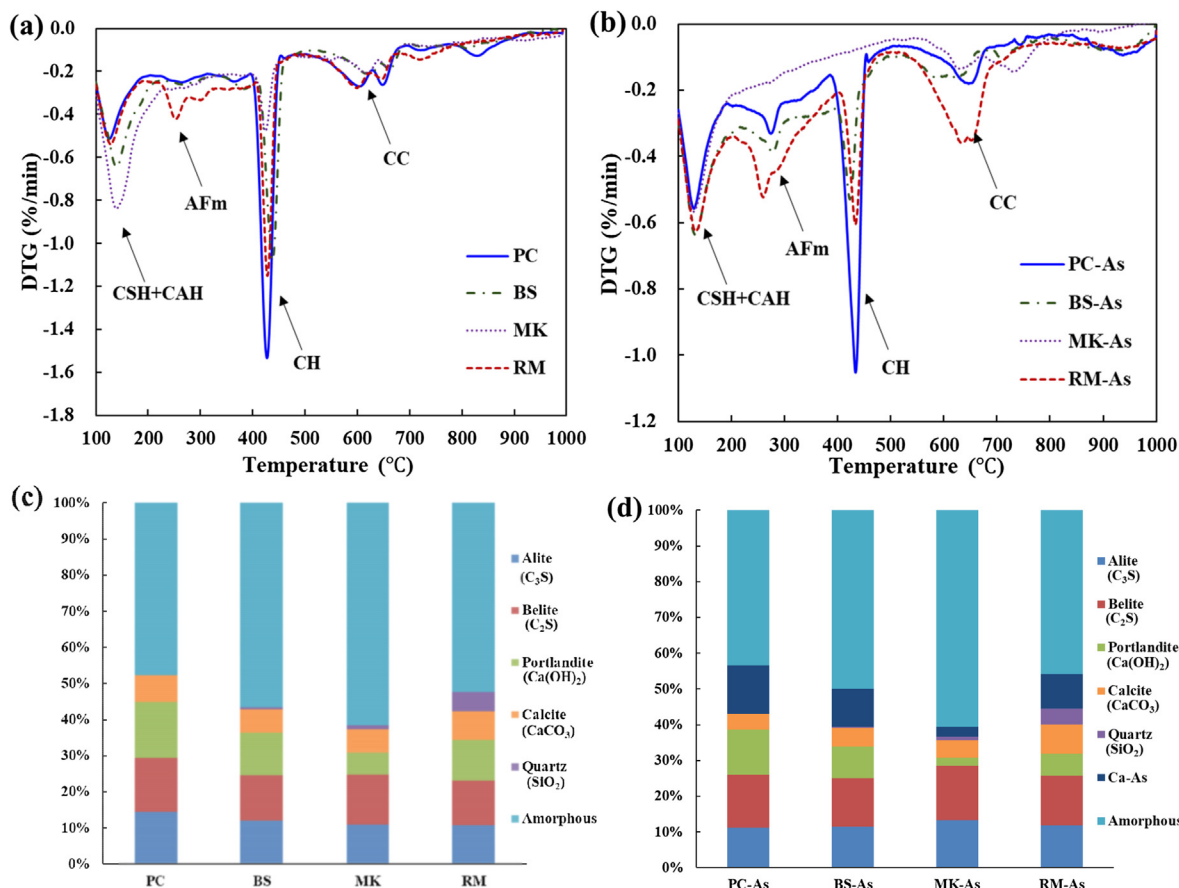
Fig. 1. TGA and QXRD of 28-d pastes with or without NaAsO$_2$: (a) DTG curves of plain pastes; (b) DTG curves of pastes with NaAsO$_2$; (c) QXRD analysis of plain pastes; (d) QXRD analysis of pastes with NaAsO$_2$.

Corundum powder (20 wt%) as an internal reference was incorporated to calculate the content of the amorphous phase in samples. The Rietveld refinement quantitative phase was analyzed by the whole powder pattern fitting method in Rigaku's integrated software (PDXL). The qualitative and quantitative analyses of Si-based samples were examined by a 400 MHz solid-state nuclear magnetic resonance spectrometer (NMR, Bruker Ascend 400 WB). ^{29}Si magic angle spinning (MAS) NMR experiments were performed on a 79.5 MHz NMR spectrometer in a 7 mm CP/MAS probe for more than 2000 scan at a rotation rate of 4500 Hz and a relaxation delay of 30 s. The deconvolution of the overlapped peaks in the NMR spectra was conducted in Origin Pro 9.0 by applying a Gaussian line model (Yu et al., 2019). The speciation of As in the powdered samples was analysed using X-ray photoelectron spectroscopy (XPS, PHI 5000 Versaprobe II) with Al Kα X-ray. A broad scan was performed with a pass energy of 187.85 eV, whereas the narrow scans of Al, Si, Ca, Fe, and As were detected with the energy of 58.7 eV. The XPS spectra were fitted by 30% Lorentzian-

Gaussian function and a Shirley baseline using the program XPSPEAK41. The sub-peaks were identified with reference to the literature based on the binding energies (NIST, 2012). The surface morphology and elemental composition of As-incorporated samples were investigated by transmission electron microscopy energy-dispersive X-ray spectroscopy (TEM-EDX, Oxford X-Max 80T). Lattice spacing of As element in the TEM image was calculated by Digital Micrograph software. The pore structure of sediment blocks after *in-situ* and *ex-situ* S/S treatment was evaluated by mercury intrusion porosimetry (MIP, Micromeritics Autopore IV), in which mercury was intruded into the freeze-dried samples (1.18–2.36 mm particles) at 207 MPa following 6.6 Pa purging in a vacuum. For quality assurance, all of the samples after 28-d air curing were crushed into the specified size and soaked in isopropanol for 7 d in total for stopping the hydration reaction (isopropanol was changed after 3-d soaking). After 7-d soaking, the samples were vacuum dried for 3 d and the homogeneously mixed samples were selected for the analytical tests.
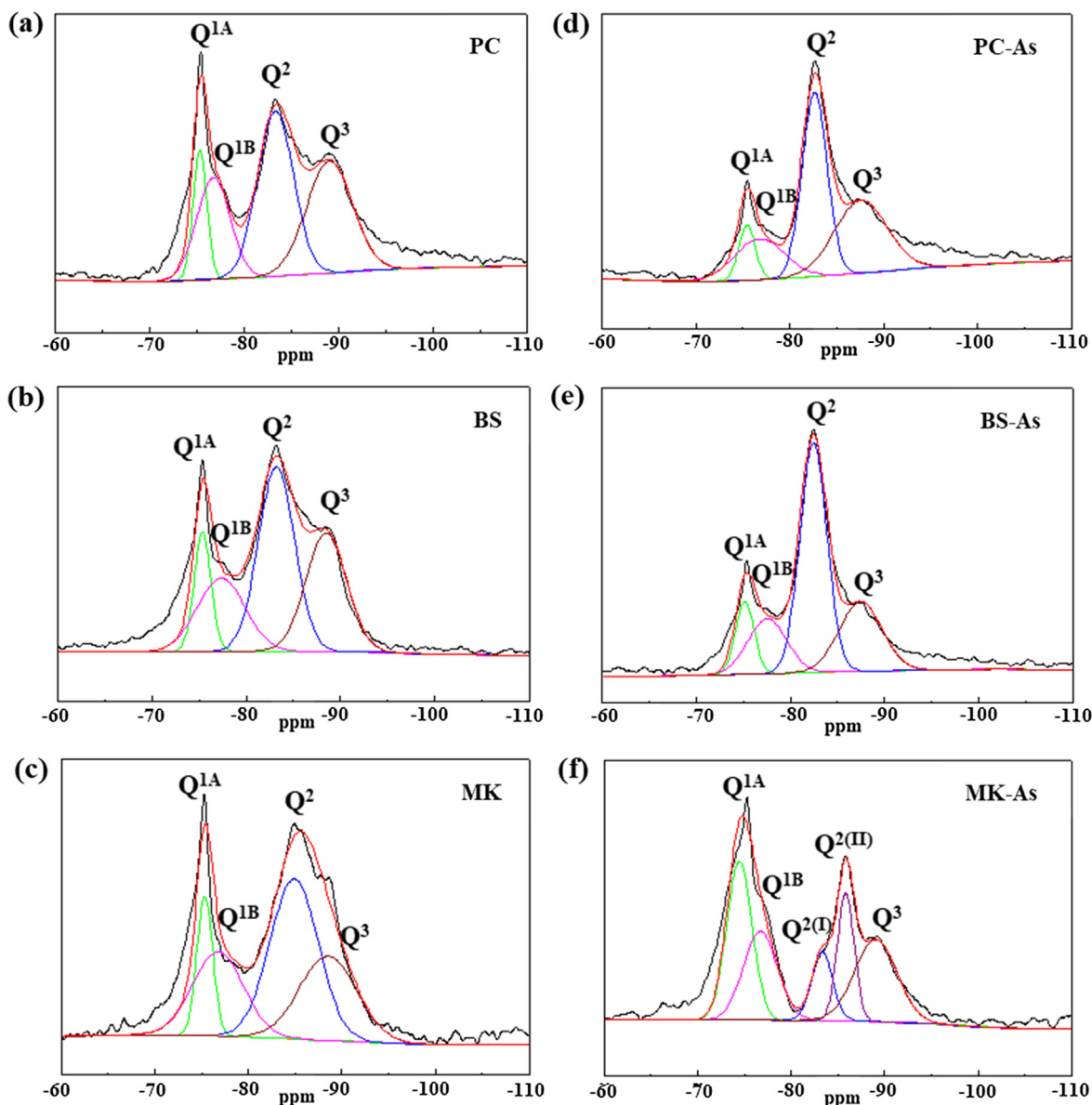
Fig. 2. ^{29}Si MAS NMR spectra of 28-d plain samples (a, b, c) or samples with $NaAsO_2$ (d, e, f).

The uniaxial compressive strength of sediment blocks after *in-situ* and *ex-situ* S/S treatment was measured triplicated by a universal testing machine (Testometric CXM 500-50 KN) at a loading rate of 0.6 MPa s^{-1} (BS EN 12390, 2009). In addition, the leachability of As from S/S samples was examined by the Toxicity Characteristic Leaching Procedure (TCLP) (US EPA, 1992). The concentrations of leaching As from different samples were measured by an inductively coupled plasma-atomic emission spectrometry (ICP-AES, Spectro Arcos). For quality assurance, samples were performed in duplicate (or in triplicate when deviation was greater than 5%). The calibration of standard concentrations was carried out prior to each analysis. Standards were analysed every 10 samples and the detection limit of As was 0.01 mg L^{-1}. The potential precipitation of As-compounds was analysed using Visual MINTEQ ver. 3.1.

3. Results and discussion

3.1. Chemical interactions of green materials during the course of as immobilization

Derivative thermogravimetry (DTG) curves of different samples with or without As are shown in Fig. 1a and b. The curve of pure PC pastes displays decomposition peaks of CSH and CAH (140 °C), CH (430 °C), and CC (550–750 °C) (Fig. 1a). The replacement of BS (20 wt%) resulted in a decrease of CH content from 19.6 wt% to 15.2 wt%, whereas it increased the contents of CSH and CAH. This indicated that the active silicon dioxide and aluminium oxide in BS reacted with hydration products (CH) to generate additional hydrates (CSH and CAH) via pozzolanic reaction, which could be favourable for the immobilization of toxic elements (Wang et al. 2018a; Zhang et al., 2019). By comparison, the incorporation of MK significantly reduced the CH content by 62% and similarly increased the contents of CSH and CAH. This was associated with a relatively high content of active silicon dioxide and aluminium oxide (97.3 wt%) in the calcined clay mineral (MK). In contrast, for RM samples, while the content of CH was
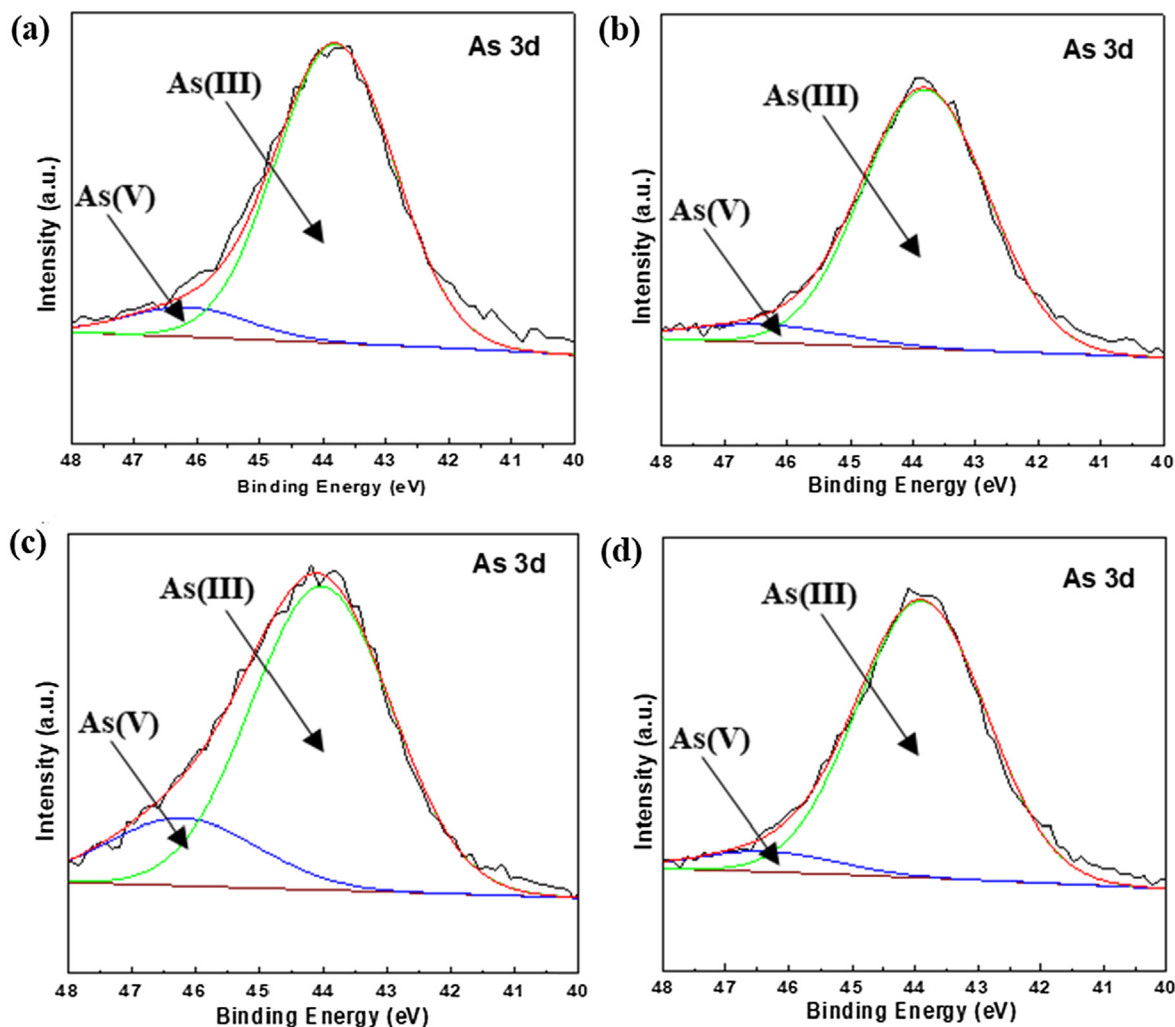
Fig. 3. As3d XPS spectra of 28-d pastes with $NaAsO_2$: (a) PC; (b) BS; (c) MK; (d) RM.

reduced, a new and remarkable peak of aluminate ferrite monosulphate (AFm) appeared at 250 °C, indicating the reaction between Fe-rich RM and cement clinker (Manfroi et al., 2014; Zhang et al., 2018a, 2018b). Therefore, the final chemical components were distinctive in different samples, although the total mass losses of four pastes were similar (19 wt%) (Fig. S1, Supplementary Information).

The QXRD results (Fig. 1c) confirmed that the green materials consumed CH to generate additional amorphous phases (i.e., CSH and CAH gels). It should be noted that the active silicon dioxide and aluminium oxide in raw materials are also in amorphous phases (Longhi et al., 2016; Wang et al., 2019b), which cannot be distinguished from the XRD patterns (Fig. S1c). However, the degree of cement hydration could be deduced from the content variations of tricalcium silicate (C_3S) and dicalcium silicate (C_2S). Incorporation of green materials slightly decreased the contents of C_3S and C_2S by 21%, whereas the CH content was significantly decreased by 28–63%. This verified that CH was partially consumed and transformed into CSH and CAH gels, especially for MK samples.

Compared to plain PC samples, the addition of 20 wt% $NaAsO_2$ led to a 22% reduction in CH content (Fig. S1b). BS samples also had a similar CH reduction after As addition. However, the CH peak in MK-As samples nearly disappeared and the contents of CSH and CAH remarkably decreased compared to those of plain MK samples. This implied that As oxyanions had complexing capacities with CH and inhibited the pH elevation. The lack of CH in MK-As pastes prevented subsequent formation of CSH and CAH, which may have an adverse

effect on As immobilization. By contrast, the presence of As had a relatively low impact on the hydration of RM samples such that the content of AFm still increased (Fig. 1b). From Fig. S1b, MK-As samples showed the lowest mass loss of hydrates while RM samples showed the highest. This further evidenced that As addition significantly inhibited the hydration of MK-incorporated binder whereas RM-incorporated binder had excellent compatibility with As. The QXRD results illustrated that approximately 24.3 wt% of C_3S and C_2S existed in MK-As samples, which were higher than that of plain MK samples. This corroborated that As severely inhibited the hydration of MK pastes, where hydration products may be insufficient for effective immobilization of As.

The hydration products of different samples with or without As were characterized by ^{29}Si NMR, except RM samples in which abundant Fe content interfered with NMR analysis. As shown in Fig. 2a, two signals at -75 and -77 ppm in PC can be considered as Q^{1A} and Q^{1B} (two different types of Q^1 ($\underline{Si}(OCa)(OSi)(OH)_2$, end-chain group in layered structure of CSH). The peak located at -83 ppm accounts for Q^2 ($\underline{Si}(OCa)(OSi)_2OH$, middle-chain group in layered structure of CSH), whereas the peak at -89 ppm is ascribed to Q^3 ($\underline{Si}(OCa)(OSi)_3$, cross-linked group in tobermorite-like CSH) (Martini et al., 2017; Wang et al., 2019c). The average degree of connectivity (Dc) in Si-based hydrates can be calculated according to the following equation (Jeong et al., 2018).
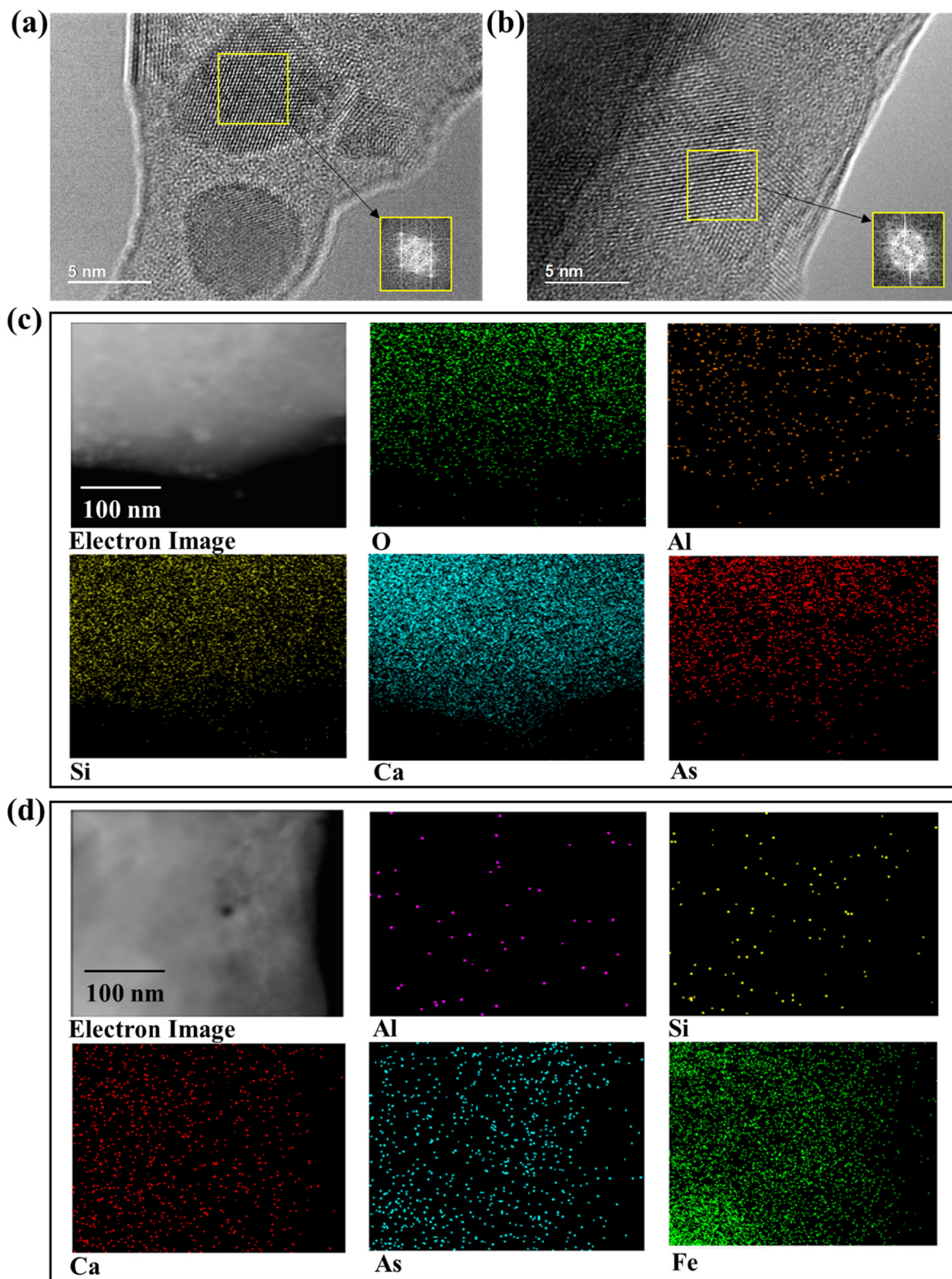
Fig. 4. TEM image with elemental mapping of pastes containing NaAsO$_2$: (a) TEM image of BS-As paste; (b) TEM image of RM-As paste; (c) element mapping of BS-As paste; (d) element mapping of RM-As paste.

$$D_C = \frac{Q^1 + 2Q^2 + 3Q^3}{Q^1 + Q^2 + Q^3}$$

A higher value of Dc indicates the higher polymerization of the Si-based hydrates. The proportional distribution of Q^1, Q^2, and Q^3 in PC pastes was approximately 32.1%, 36.4%, and 31.5%, respectively. The

BS-incorporated samples showed similar proportional distribution of silicon types (Fig. 2b). The incorporation of MK resulted in a decrease of Q^3 phase but an increase of Q^2 phase (Fig. 2c), suggesting the relatively weak polymerization of hydrates in MK samples. In the presence of As, Q^2 was the dominant type of silicon in PC-As and BS-As samples (40.7–49.1%) (Fig. 2d&e), while the Q^1 phase occupied the largest
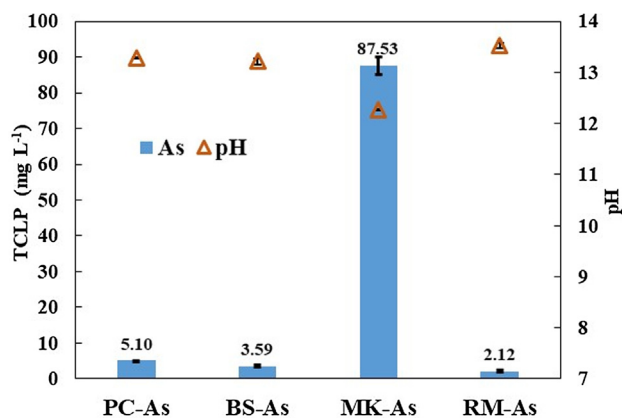
Fig. 5. TCLP As leaching concentrations of pastes containing 20 wt% NaAsO₂.

proportion (50.1%) in MK-As samples (Fig. 2f). This evidenced that the immobilization of As not only inhibited the hydration degree but also reduced the polymerization of hydrates in MK-incorporated samples, which may have an adverse influence on S/S performance.

XPS spectra (Fig. 3a) show that As(III) at the binding energy of 43.8 eV was the dominant speciation of As in the S/S samples. Approximately 9.2% of As in the PC samples was oxidized to As(V) at the binding energy of 46.2 eV (Li et al., 2018; Zhong et al., 2019). Such transformation from As(III) to As(V) is favourable for the immobilization of As, because As(V) is more stable and less toxic than As(III) (Xiu et al., 2016). The proportions of As(V) in BS- and RM-incorporated samples were comparable to that of the PC samples. However, 19.4% of As was oxidized in MK-incorporated samples, which may be associated

with the redox conditions in the MK systems (Wang et al., 2014). Besides, the binding energy of As(III) was shifted to 44.0 eV, suggesting new coordination between As and other elements. Based on the XPS spectra of Al, Si, and Ca (Fig. S2–S4), the major difference among the four samples was the relatively high content of Al 2p₁/₂ at 75.7 eV in MK-incorporated samples, which may engage in the coordination with As (Debure et al., 2018; Penke et al., 2019). For Fe-rich RM-incorporated samples (Fig. S5), As(III) oxidation was insignificant, although As(III) may be photo-oxidized into As(V) in the presence of dissolved Fe with light induction (Gomaa et al., 2017). It is widely recognized that Fe(II) and Fe(III) have strong sorption affinity of As(III) and As(V) via inner-sphere complexation (Sun et al., 2017). Thus, the RM incorporation may enhance the chemical fixation of As.

From the TEM image (Fig. 4a), the spots blended perfectly into the matrix of BS-As samples. The spots show a striated contrast with the lattice spacing of 0.188 nm and remarkable symmetrical bright points can be observed from the electron diffraction pattern, suggesting that the high-density and well-crystallized As-compounds were wrapped by hydrates (Lei et al., 2018). According to the elemental mapping results (Fig. 4c), the distribution of As presented a positive correlation with Ca, signifying the precipitation of Ca-As compounds, which augmented the XRD results. For the TEM image of RM samples (Fig. 4b), the spot surface shows relatively rough contrast with a circular electron diffraction pattern, indicating the amorphous type of As-compounds in the hydrates (Berre et al., 2008). As illustrated in Fig. 4d and Fig. S6, the presence of As was accompanied by Ca and Fe, which reinforced the significance of coordination and stabilization of As by Fe-rich RM.

As illustrated from Fig. 5, the TCLP leaching concentration of As from the PC S/S samples was 5.10 mg L⁻¹. The addition of BS resulted in a further reduction by 29.6% in the As leachability to 3.59 mg L⁻¹, which was attributed to the generation of additional CSH and CAH gels
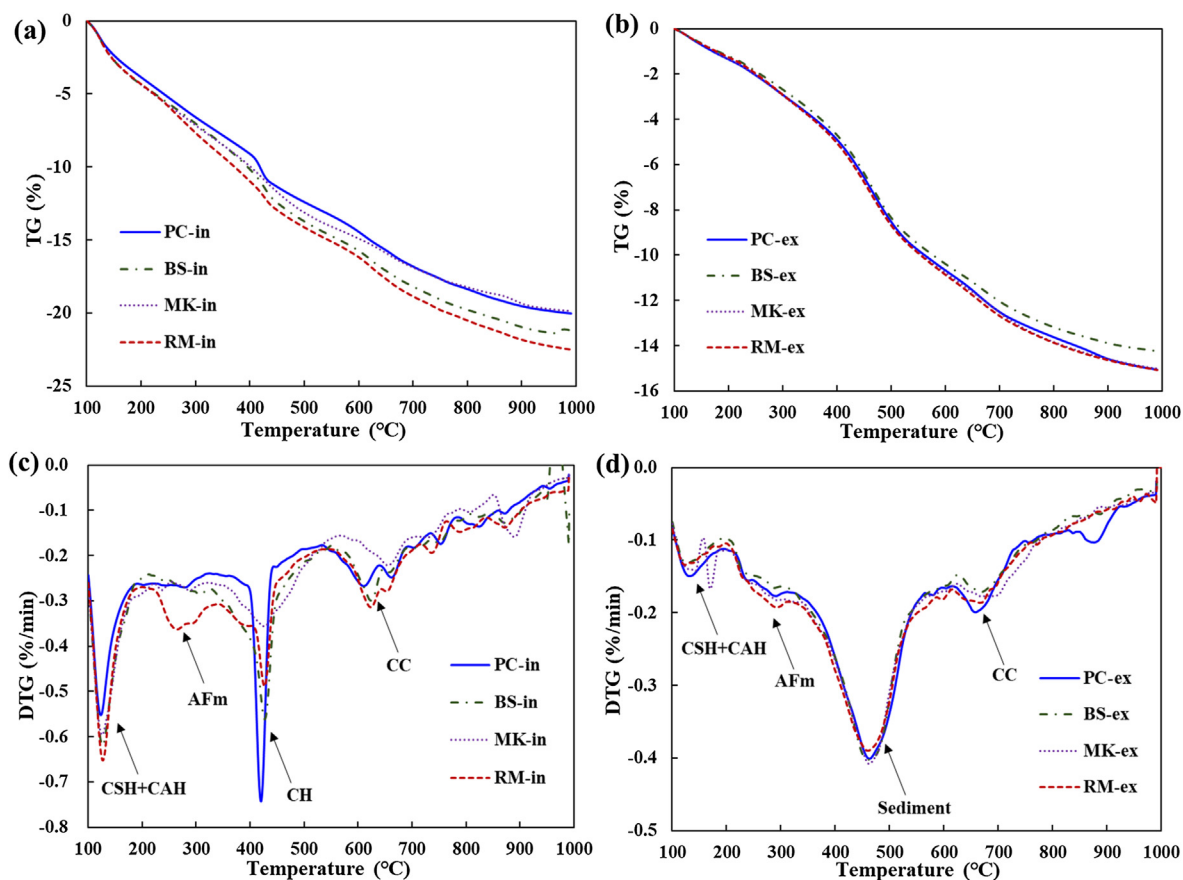
Fig. 6. TGA analysis of 28-d *in-situ* and *ex-situ* S/S sediment blocks: (a) TG curves of *in-situ* S/S blocks; (b) TG curves of *ex-situ* S/S blocks; (c) DTG curves of *in-situ* S/S blocks; (d) DTG curves of *ex-situ* S/S blocks;
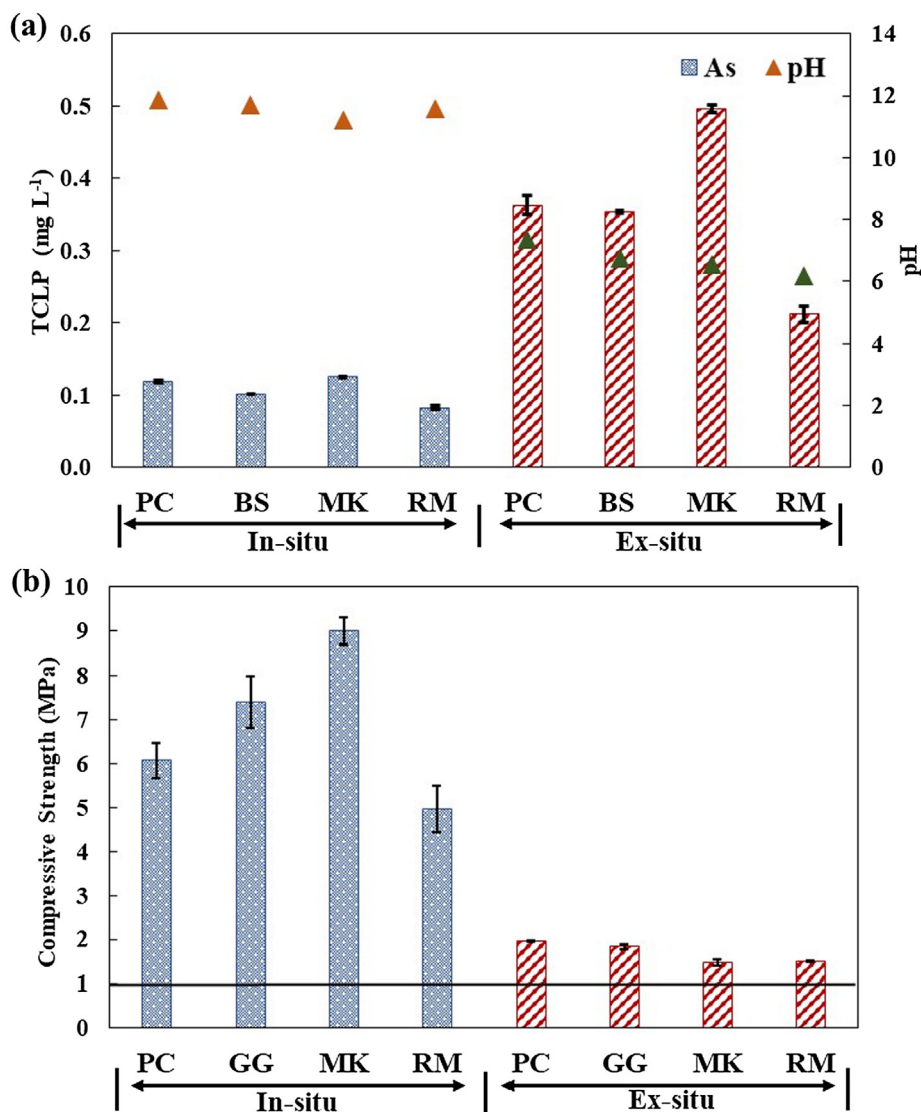
Fig. 7. TCLP As leachability (a) and compressive strength (b) of 28-d *in-situ* and *ex-situ* S/S sediment blocks.

for As immobilization as revealed by XRD and TGA analyses. The RM-incorporated samples presented the lowest As leachability (2.12 mg L^{-1}, i.e., 99.88% S/S efficiency), owing to the strong complexation ability of Fe with As. By contrast, it was unexpected that the addition of MK dramatically increased the As leachability by 16.2 times (i.e., 97.73% S/S efficiency). Although the pH value of 12.3 was within the As precipitation range of Ca-O-As (pH 7.9-13.4) according to previous results (Beak and Wilkin, 2009; Wang et al., 2019b), the CH deficiency and limited amounts of CSH and CAH in the MK-incorporated samples may lead to the high leachability of As under elevated alkalinity, which was also observed in the PC S/S systems (Li et al., 2018). To validate the S/S efficiency in practical engineering applications, four binders were employed for the *in-situ* and *ex-situ* S/S of As-contaminated sediment.

3.2. Waste-incorporated binders for In-situ and Ex-situ S/S of As-contaminated sediment

Among *in-situ* S/S sediment samples (30% binder and 70% sediment), RM-incorporated samples showed the highest content of hydrates, which was followed by BS-incorporated samples as revealed by the TG curves (Fig. 6a). Due to the relatively low content of As (28.3 mg kg^{-1}) in the *in-situ* S/S samples, the presence of As had a less significant inhibitory effect on the generation of total hydrates in MK-

incorporated samples, although the CH content was relatively low as indicated by the DTG curves (Fig. 6c) and XRD patterns (Fig. S7a). As for the *ex-situ* S/S samples (10% binder and 90% sediment), there were remarkable peaks between 350 °C and 450 °C associated with the decomposition of organic matter in the sediment (Fig. 6d) (Wang et al., 2018a). The strong Ca-complexing ability of organic matter significantly inhibited the hydration process (Wang et al., 2015) and resulted in the reduction of hydrates content (Fig. 6b), which was also evidenced by the XRD results (Fig. S7b). From the MIP results (Fig. S8a), PC, BS-incorporated, and RM-incorporated samples showed similar pore size distribution. By comparison, MK-incorporated samples had relatively low pore volume, especially in the range of capillary pores. This may be attributed to the fine particle size of MK and additional CSH and CAH gels for pore filling (Wu et al., 2016). In addition, the cumulative intrusion volume of *ex-situ* S/S sediment blocks was approximately 2.66 times larger than that of *in-situ* S/S samples (Fig. S8b), corresponding to the amounts of sediment (Wang et al., 2018a). The As inhibition on the pozzolanic reaction in MK-incorporated and BS-incorporated samples might also be responsible for the enlarged porosity.

The TCLP results (Fig. 7a) illustrated that the leaching concentrations of As from *in-situ* S/S sediment samples were between 0.08 mg L^{-1} and 0.13 mg L^{-1}, which represented only 0.59–0.89% of As

leaching concentrations from untreated sediment. The MK-incorporated samples showed a comparable As leachability with PC samples, while the former had the highest compressive strength (9.01 MPa) (Fig. 7b) owing to additional hydrates and dense structure (Fig. S8a). Compared to *in-situ* S/S samples, *ex-situ* S/S samples presented much higher As leachability. MK-incorporated samples showed the highest As leaching concentration (0.50 mg L^{-1}), whereas RM-incorporated samples showed the lowest value (0.21 mg L^{-1}), which was in line with the above discussion. The As leachability of all the *ex-situ* samples fulfilled universal treatment standards (5 mg L^{-1}) and all the samples confirmed with strength requirement (1 MPa) for the reuse as fill materials (Li et al., 2018). It should be noted that TCLP may underestimate the leaching of As from the S/S samples, as the condition of alkaline pH, low redox potential, and biological activity may also facilitate As leaching (Ghosh et al., 2004; Beiyuan et al., 2017b). Recent studies further suggested that well-controlled S/S products of dredged sediment via *ex-situ* S/S treatment can be valorized as construction building materials, such as backfill materials (low-quality), partition blocks (medium-quality), and paving blocks (high-quality) (Wang et al., 2018a; Wang et al., 2019d), whereas the undredged sediment via *in-situ* S/S treatment can be utilized as foundation for marine reclamation with the use of super-fast marine dredging and rainbow-filling technology (Zhu et al., 2018). In view of the performance of As immobilization and mechanical strength, RM-incorporated binder can be used for low-cost and low-carbon S/S treatment of high-As contaminated waste with minimum leachability, whereas MK-incorporated binder can be suitable for immobilizing low-As waste and achieving superior mechanical strength.

4. Conclusions

This study investigated the efficacy and mechanistic roles of BS, MK, and RM for green and sustainable stabilization/solidification (S/S) of As-contaminated sediment. TGA and QXRD analyses illustrated that BS and MK reacted with hydrated CH to generate additional CSH and CAH via the pozzolanic reaction, whereas RM engaged in hydration reaction to generate AFm. In MK-incorporated samples, ^{29}Si NMR illustrated that As not only hindered the hydration degree but also reduced the polymerization of hydrates. By contrast, RM-incorporated binder demonstrated excellent compatibility with As via Fe-As complexation as revealed by XPS. TEM image and elemental mapping results showed the positive correlation between the distribution of As and that of Ca and Fe, signifying the precipitation of crystalline Ca-As and amorphous Fe-As compounds. As a result, MK-As samples showed the lowest efficiency of As immobilization whereas RM-As samples provided the highest efficiency for *in-situ* and *ex-situ* sediment S/S treatment. For practical application, the durability of S/S products under different field-relevant physical, chemical, and biological conditions should be further validated in future studies. Overall, waste valorization of red mud as a green and low-carbon additive is plausible for actualizing sustainable remediation of As-contaminated sediment.

Declaration of Competing Interest

The authors declare that they have no known competing financial interests or personal relationships that could have appeared to influence the work reported in this paper.

Appendix A. Supplementary material

Supplementary data to this article can be found online at https://doi.org/10.1016/j.envint.2019.105247.

References

Aghadadashi, V., Neyestani, M.R., Mehdinia, A., Riyahi Bakhtiari, A., Molaei, S., Farhangi, M., Esmaili, M., Rezai Marnani, H., Gerivani, H., 2019. Spatial distribution and vertical profile of heavy metals in marine sediments around Iran's special economic energy zone; Arsenic as an enriched contaminant. Mar. Pollut. Bull. 437–450.

Avet, F., Li, X., Scrivener, K., 2018. Determination of the amount of reacted metakaolin in calcined clay blends. Cem. Concr. Res. 106, 40–48.

Beak, D.G., Wilkin, R.T., 2009. Performance of a zerovalent iron reactive barrier for the treatment of arsenic in groundwater: Part 2. Geochemical modeling and solid phase studies. J. Contam. Hydrol. 106, 15–28.

Beiyuan, J., Li, J.S., Tsang, D.C.W., Wang, L., Poon, C.S., Li, X.D., Fendorf, S., 2017a. Fate of arsenic before and after chemical-enhanced washing of an arsenic-containing soil in Hong Kong. Sci. Total Environ. 599–600, 679–688.

Beiyuan, J., Awad, Y.M., Beckers, F., Tsang, D.C.W., Ok, Y.S., Rinklebe, J., 2017b. Mobility and phytoavailability of As and Pb in a contaminated soil using pine sawdust biochar under systematic change of redox conditions. Chemosphere 178, 110–118.

Bettoschi, A., Marrucci, A., Marras, B., Atzori, M., Schintu, M., 2018. Arsenic speciation in marine sediments: a comparison between two sequential extraction procedures. Soil Sediment Contam. 27, 723–735.

BS EN 12390, 2009. Testing Hardened Concrete Compressive Strength of Test. Specimens. British Standards Institution, London, United Kingdom.

Cai, C., Zhao, M., Yu, Z., Rong, H., Zhang, C., 2019. Utilization of nanomaterials for in-situ remediation of heavy metal (loid) contaminated sediments: a review. Sci. Total Environ.

Chen, L., Wang, L., Cho, D.-W., Tsang, D.C.W., Tong, L., Zhou, Y., Yang, J., Hu, Q., Poon, C.S., 2019a. Sustainable stabilization/solidification of municipal solid waste incinerator fly ash by incorporation of green materials. J. Clean. Prod. 222, 335–343.

Chen, M., Ding, S., Gao, S., Fu, Z., Tang, W., Wu, Y., Gong, M., Wang, D., Wang, Y., 2019b. Efficacy of dredging engineering as a means to remove heavy metals from lake sediments. Sci. Total Environ. 665, 181–190.

Jinli Cui, Chuanyong Jing. A review of arsenic interfacial geochemistry in groundwater and the role of organic matter.

Debure, M., Tournassat, C., Lerouge, C., Madé, B., Robinet, J.C., Fernández, A.M., Grangeon, S., 2018. Retention of arsenic, chromium and boron on an outcropping clay-rich rock formation (the Tégulines Clay, eastern France). Sci. Total Environ. 642, 216–229.

Ding, S., Chen, M., Gong, M., Fan, X., Qin, B., Xu, H., Gao, S.S., Jin, Z., Tsang, D.C.W., Zhang, C., 2018. Internal phosphorus loading from sediments causes seasonal nitrogen limitation for harmful algal blooms. Sci. Total Environ. 625, 872–884.

Garcia-Ordiales, E., Covelli, S., Rico, J.M., Roqueñí, N., Fontolan, G., Flor-Blanco, G., Cienfuegos, P., Loredo, J., 2018. Occurrence and speciation of arsenic and mercury in estuarine sediments affected by mining activities (Asturias, northern Spain). Chemosphere 198, 281–289.

Gbozee, M., Zheng, K., He, F., Zeng, X., 2018. The influence of aluminum from metakaolin on chemical binding of chloride ions in hydrated cement pastes. Appl. Clay Sci. 158, 186–194.

Ghosh, A., Mukiibi, M., Ela, W., 2004. TCLP underestimates leaching of arsenic from solid residuals under landfill conditions. Environ. Sci. Technol. 38, 4677–4682.

Gomaa, H., Khalifa, H., Selim, M.M., Shenashen, M.A., Kawada, S., Alamoudi, A.S., Azzam, A.M., Alhamid, A.A., El-Safty, S.A., 2017. Selective, photoenhanced trapping/detrapping of arsenate anions using mesoporous blobfish head TiO$_2$ monoliths. ACS Sustain. Chem. Eng. 5, 10826–10839.

Hammond, C.M., Root, R.A., Maier, R.M., Chorover, J., 2018. Mechanisms of Arsenic Sequestration by Prosopis juliflora during the Phytostabilization of Metalliferous Mine Tailings. Environ. Sci. Technol. 52, 1156–1164.

He, Z., Zhu, X., Wang, J., Mu, M., Wang, Y., 2019. Comparison of CO$_2$ emissions from OPC and recycled cement production. Constr. Build. Mater. 211, 965–973.

HKEPD, 2018. Marine Water Quality in Hong Kong in 2017. Environmental Protection Department, Hong Kong, 2018.

Jeong, Y.J., Youm, K.S., Yun, T.S., 2018. Effect of nano-silica and curing conditions on the reaction rate of class G well cement exposed to geological CO$_2$-sequestration conditions. Cem. Concr. Res. 109, 208–216.

Kavitha, O.R., Shanthi, V.M., Arulraj, G.P., Sivakumar, V.R., 2016. Microstructural studies on eco-friendly and durable self-compacting concrete blended with metakaolin. Appl. Clay Sci. 124, 143–149.

Kim, H.T., Lee, T.G., 2017. A simultaneous stabilization and solidification of the top five most toxic heavy metals (Hg, Pb, As, Cr, and Cd). Chemosphere 178, 479–485.

Le Berre, J.F., Gauvin, R., Demopoulos, G.P., 2008. A study of the crystallization kinetics of scorodite via the transformation of poorly crystalline ferric arsenate in weakly acidic solution. Colloids Surfaces A Physicochem. Eng. Asp. 315, 117–129.

LeMonte, J.J., Stuckey, J.W., Tappero, R., Rinklebe, J., Sparks, D.L., 2017. Sea level rise induced arsenic release from historically contaminated coastal soils. Environ. Sci. Technol. 51, 5913–5922.

Lei, J., Peng, B., Liang, Y.J., Min, X.B., Chai, L.Y., Ke, Y., You, Y., 2018. Effects of anions on calcium arsenate crystalline structure and arsenic stability. Hydrometallurgy 177, 123–131.

Li, J.S., Wang, L., Cui, J.L., Poon, C.S., Beiyuan, J., Tsang, D.C.W., Li, X.D., 2018. Effects of low-alkalinity binders on stabilization/solidification of geogenic As-containing

soils: spectroscopic investigation and leaching tests. Sci. Total Environ. 631–632, 1486–1494.

Liu, J.J., Diao, Z.H., Xu, X.R., Xie, Q., Ni, Z.X., 2019. In situ arsenic speciation and the release kinetics in coastal sediments: A case study in Daya Bay, South China Sea. Sci. Total Environ. 650, 2221–2230.

Liu, L., Li, W., Song, W., Guo, M., 2018. Remediation techniques for heavy metal-contaminated soils: Principles and applicability. Sci. Total Environ. 633, 206–219.

Longhi, M.A., Rodríguez, E.D., Bernal, S.A., Provis, J.L., Kirchheim, A.P., 2016. Valorisation of a kaolin mining waste for the production of geopolymers. J. Clean. Prod. 115, 265–272.

Maletić, S.P., Beljin, J.M., Rončević, S.D., Grgić, M.G., Dalmacija, B.D., 2019. State of the art and future challenges for polycyclic aromatic hydrocarbons is sediments: sources, fate, bioavailability and remediation techniques. J. Hazard. Mater. 365, 467–482.

Manfroi, E.P., Cheriaf, M., Rocha, J.C., 2014. Microstructure, mineralogy and environmental evaluation of cementitious composites produced with red mud waste. Constr. Build. Mater. 67, 29–36.

Martini, F., Tonelli, M., Geppi, M., Ridi, F., Borsacchi, S., Calucci, L., 2017. Hydration of MgO/SiO2 and Portland cement mixtures: a structural investigation of the hydrated phases by means of X-ray diffraction and solid state NMR spectroscopy. Cem. Concr. Res. 102, 60–67.

Myers, R.J., Bernal, S.A., Provis, J.L., 2017. Phase diagrams for alkali-activated slag binders. Cem. Concr. Res. 95, 30–38.

NIST, 2012. NIST X-ray Photoelectron Spectroscopy Database. < http://srdata.nist.gov/xps/ > .

Penke, Y.K., Anantharaman, G., Ramkumar, J., Kar, K.K., 2019. Redox synergistic Mn-Al-Fe and Cu-Al-Fe ternary metal oxide nano adsorbents for arsenic remediation with environmentally stable As(0) formation. J. Hazard. Mater. 364, 519–530.

Prentice, D.P., Walkley, B., Bernal, S.A., Bankhead, M., Hayes, M., Provis, J.L., 2019. Thermodynamic modelling of BFS-PC cements under temperature conditions relevant to the geological disposal of nuclear wastes. Cem. Concr. Res. 119, 21–35.

Provis, J.L., 2018. Alkali-activated materials. Cem. Concr. Res. 114, 40–48.

Reddy, V.A., Solanki, C.H., Kumar, S., Reddy, K.R., Du, Y.J., 2019. New ternary blend limestone calcined clay cement for solidification/stabilization of zinc contaminated soil. Chemosphere 235, 308–315.

Ruan, S., Unluer, C., 2017. Influence of supplementary cementitious materials on the performance and environmental impacts of reactive magnesia cement concrete. J. Clean. Prod. 159, 62–73.

Shen, Z., Hou, D., Xu, W., Zhang, J., Jin, F., Zhao, B., Pan, S., Peng, T., Alessi, D.S., 2018. Assessing long-term stability of cadmium and lead in a soil washing residue amended with MgO-based binders using quantitative accelerated ageing. Sci. Total Environ. 643, 1571–1578.

Smith, R., Knight, R., Fendorf, S., 2018. Overpumping leads to California groundwater arsenic threat. Nat. Commun. 9, 2089.

Sun, J., Prommer, H., Siade, A.J., Chillrud, S.N., Mailloux, B.J., Bostick, B.C., 2018. Model-based analysis of arsenic immobilization via iron mineral transformation under advective flows. Environ. Sci. Technol. 52, 9243–9253.

Sun, Q., Ding, S., Chen, M., Gao, S., Lu, G., Wu, Y., Gong, M., Wang, D., Wang, Y., 2019a. Long-term effectiveness of sediment dredging on controlling the contamination of arsenic, selenium, and antimony. Environ. Pollut. 245, 725–734.

Sun, Y., Lei, C., Khan, E., Chen, S.S., Tsang, D.C.W., Ok, Y.S., Lin, D., Feng, Y., Li, X. dong, 2017. Nanoscale zero-valent iron for metal/metalloid removal from model hydraulic fracturing wastewater. Chemosphere 176, 315–323.

Sun, Y., Yu, I.K.M., Tsang, D.C.W., Cao, X., Lin, D., Wang, L., Graham, N.J.D., Alessi, D.S., Komárek, M., Ok, Y.S., Feng, Y., Li, X.D., 2019b. Multifunctional iron-biochar composites for the removal of potentially toxic elements, inherent cations, and heterochloride from hydraulic fracturing wastewater. Environ. Int. 521–532.

Tian, N., Tian, X., Liu, X., Zhou, Z., Yang, C., Ma, L., Tian, C., Li, Y., Wang, Y., 2016. Facile synthesis of hierarchical dendrite-like structure iron layered double hydroxide

nanohybrids for effective arsenic removal. Chem. Commun. 52, 11955–11958.

US EPA, M, 1992. Toxicity Characteristic Leaching Procedure. U.S. Environmental Protection Agency, Washington, DC, USA.

Wang, L., Tsang, D.C.W., Poon, C.S., 2015. Green remediation and recycling of contaminated sediment by waste-incorporated stabilization/solidification. Chemosphere 122, 257–264.

Wang, L., Chen, L., Tsang, D.C.W., Li, J.S., Baek, K., Hou, D., Ding, S., Poon, C.S., 2018a. Recycling dredged sediment into fill materials, partition blocks, and paving blocks: technical and economic assessment. J. Clean. Prod. 199, 69–76.

Wang, L., Yu, K., Li, J.S., Tsang, D.C.W., Poon, C.S., Yoo, J.C., Baek, K., Ding, S., Hou, D., Dai, J.G., 2018b. Low-carbon and low-alkalinity stabilization/solidification of high-Pb contaminated soil. Chem. Eng. J. 351, 418–427.

Wang, L., Chen, S.S., Sun, Y.Q., Tsang, D.C.W., Yip, A.C.K., Ding, S.M., Hou, D.Y., Baek, K., Ok, Y.S., 2019a. Efficacy and limitations of low-cost adsorbents for in-situ stabilization of contaminated marine sediment. J. Clean. Prod. 212, 420–427.

Wang, L., Cho, D.W., Tsang, D.C.W., Cao, X., Hou, D., Shen, Z., Alessi, D.S., Ok, Y.S., Poon, C.S., 2019b. Green remediation of As and Pb contaminated soil using cement-free clay-based stabilization/solidification. Environ. Int. 126, 336–345.

Wang, L., Chen, L., Cho, D.W., Tsang, D.C.W., Yang, J., Hou, D., Baek, K., Kua, H.W., Poon, C.S., 2019c. Novel synergy of Si-rich minerals and reactive MgO for stabilisation/solidification of contaminated sediment. J. Hazard. Mater. 695–706.

Wang, L., Chen, L., Tsang, D.C.W., Kua, H.W., Yang, J., Ok, Y.S., Ding, S.M., Hou, D.Y., Poon, C.S., 2019d. The roles of biochar as green admixture for sediment-based construction products. Cement Concrete Comp. 104, 103348.

Wang, Y., Morin, G., Ona-Nguema, G., Brown, G.E., 2014. Arsenic(III) and arsenic(V) speciation during transformation of lepidocrocite to magnetite. Environ. Sci. Technol. 48, 14282–14290.

Wu, Z., Deng, Y., Liu, S., Liu, Q., Chen, Y., Zha, F., 2016. Strength and micro-structure evolution of compacted soils modified by admixtures of cement and metakaolin. Appl. Clay Sci. 127–128, 44–51.

Xie, J., Wang, J., Zhang, B., Fang, C., Li, L., 2019. Physicochemical properties of alkali activated GGBS and fly ash geopolymeric recycled concrete. Constr. Build. Mater. 204, 384–439.

Xiu, W., Guo, H., Shen, J., Liu, S., Ding, S., Hou, W., Ma, J., Dong, H., 2016. Stimulation of Fe(II) Oxidation, Biogenic Lepidocrocite Formation, and Arsenic Immobilization by Pseudogulbenkiania Sp. Strain 2002. Environ. Sci. Technol. 50, 6449–6458.

Yoo, J.C., Beiyuan, J., Wang, L., Tsang, D.C.W., Baek, K., Bolan, N.S., Ok, Y.S., Li, X.D., 2018. A combination of ferric nitrate/EDDS-enhanced washing and sludge-derived biochar stabilization of metal-contaminated soils. Sci. Total Environ. 616–617, 572–582.

Yu, I.K.M., Xiong, X., Tsang, D.C.W., Wang, L., Hunt, A.J., Song, H., Shang, J., Ok, Y.S., Poon, C.S., 2019. Aluminium-biochar composites as sustainable heterogeneous catalysts for glucose isomerisation in a biorefinery. Green Chem. 21, 1267–1281.

Zhang, B., Wei, J., Zeng, Z., Xu, W., Yu, Q., 2018a. Effects of sulfur on the solidification of cadmium during clinkerization. ACS Sustain. Chem. Eng. 6, 10645–10653.

Zhang, Y., Chang, J., Ji, J., 2018b. AH3 phase in the hydration product system of AFt-AFm-AH3 in calcium sulfoaluminate cements: a microstructural study. Constr. Build. Mater. 167, 587–596.

Zhang, Y., Zhang, S., Ni, W., Yan, Q., Gao, W., Li, Y., 2019. Immobilisation of high-arsenic-containing tailings by using metallurgical slag-cementing materials. Chemosphere 223, 117–123.

Zhong, D., Jiang, Y., Zhao, Z., Wang, L., Chen, J., Ren, S., Liu, Z., Zhang, Y., Tsang, D.C.W., Crittenden, J.C., 2019. pH dependence of arsenic oxidation by rice-husk-derived biochar: roles of redox-active moieties. Environ. Sci. Technol. 53, 9034–9044.

Zhu, W., Yan, J., Yu, G., 2018. Vacuum preloading method for land reclamation using hydraulic filled slurry from the sea: a case study in coastal China. Ocean Eng. 152, 286–299.